


# Effect of layer thickness for the bounce of a particle settling through a density transition layer

Shuhong Wang, Jiadong Wang, and Jian Deng <sup>\*</sup>

*Department of Mechanics, Zhejiang University, Hangzhou 310027, People's Republic of China*



(Received 11 January 2023; revised 9 June 2023; accepted 4 December 2023; published 28 December 2023)

We study numerically a spherical particle settling through a density transition layer at moderate Reynolds numbers  $Re_u = 69 \sim 259$  for the upper fluid. We investigate how the transition layer thickness affects the particle's bouncing behavior as it crosses the interface. The previous intuitive understanding was that the bounce occurs when the relative thickness of the transition layer,  $L/D$ , which is characterized by the ratio of the layer thickness  $L$  to the particle diameter  $D$ , is small. Indeed, we report no bounce phenomenon for very thick interfaces, i.e.,  $L/D > 10$  in the current parametric range. However, we argue that the bounce can also be inhibited when  $L/D$  is too small. Upon a fixed upper layer Reynolds number  $Re_u = 207$  with varying  $L/D$ , we examine the flow evolution of these cases. We propose that this inhibition is attributed to two mechanisms. First, as the interface thickness decreases, the detachment of the attached lighter fluid from the upper layer occurs more rapidly, resulting in a faster decrease in buoyancy. Second, in the case of a very thin interface ( $L/D = 0.5\text{--}3.0$ ), the residual light fluid accumulates and undergoes a secondary detachment, separating from the particle at an angle relative to the central axis. This secondary detachment reduces the drag force and effectively prevents the particle from experiencing a rebound motion.

DOI: [10.1103/PhysRevE.108.065108](https://doi.org/10.1103/PhysRevE.108.065108)

## I. INTRODUCTION

In oceans and lakes, fluid is commonly stratified due to the nonuniform distribution of temperature and salinity in height. Objects moving vertically in such a circumstance lead to the fluid dynamics significantly different from that in a homogeneous fluid, such as the formation of rear vertical jets [1–3], generation of internal waves [1,4,5], enhancement of drag force [6,7], dragging and rupture of isopycnals [8–11]. Due to the wide applications in many environmental and engineering processes, including the spread of marine pollutants, the dispersion of spilled oil, the sedimentation of marine snow particles, and the transportation and operation of underwater vehicles, the interaction between vertically moving objects and their ambient stratified fluid has attracted a certain interest over the last decades. These studies have been recently reviewed [12,13].

In three-layer stratified fluid, a settling particle tends to distort the isopycnals and drag light fluid from the upper layer into the stratified region, thus increasing substantially the drag on it and decelerating it within the stratified layer [10]. At low Reynolds numbers ( $Re \sim 1\text{--}10$ ), the enhanced drag can be estimated by the buoyancy of a finite volume of the attached light fluid [10]. In a continuously stratified fluid, Yick *et al.* [6] proposed that a shell of fluid around the particle with the width  $\delta \sim (\nu/N)^{1/2}$  determines the added drag. Verso *et al.* [11] modeled the transient drag as a particle passes through a density interface by considering an initially constant wake volume with value  $V_{c0} \sim 0.13Fr^{3/4}V_p$  and reduces exponentially after passing the interface. For extremely low Reynolds

numbers, i.e.,  $Re \ll 1$ , fundamental solutions considering a point force (Stokeslet) were proposed, which demonstrate the existence of a fundamental stratification length scale, which is governed by a competition between buoyancy, diffusion and viscosity [14]. It was noted that the particles as small as  $O(100\text{ }\mu\text{m}\text{--}1\text{ mm})$  can also be influenced by stratification.

At moderate Reynolds numbers ( $Re \sim 100$ ), Torres *et al.* [1] found that the standing vortex occurring in a homogeneous fluid collapses in the linearly stratified fluid, forming a strong upward jet. This jet causes a reduction of the pressure on the rear surface of the particle, which leads to the increase in pressure drag. The jet structure was studied comprehensively by towing a sphere vertically at constant speeds in a salt-stratified fluid, over a wide parametric range of  $30 \leq Re \leq 4000$  and  $0.2 \leq Fr \leq 70$  [2]. According to their experiments, the wake structures were classified into different types, including two types of thin jets, the one with bell-shaped structure, those with periodically generated knots, a simply meandering jet, and a turbulent jet. The velocity distribution of the bell-shaped jet structure was investigated numerically by Hanazaki *et al.* [3] and experimentally by Okino *et al.* [15]. They found that the jet length is determined by the vertical wavelength of the internal waves, scaled as  $\pi Fr/2$ , and the jet radius is scaled by  $\sqrt{Fr/2Re}$ . At  $Fr \leq 0.2$ , the strong stratification promotes the transition of stable jets into the turbulence regime, even at relatively low Reynolds numbers, e.g.,  $10 \leq Re \leq 100$  [16].

The deflected isopycnals lead to a new vorticity generation term, the so-called baroclinic torque, given as  $\mathbf{T}_g = \nabla p \times \nabla(\frac{1}{\rho})$  [5,13]. The baroclinic torque leads to orientation instability in the settling of nonspherical particles, such as elongated particles and disks [17–20]. In addition, the baroclinic vorticity also contributes to the drag enhancement by elevating the shear stress at the particle's surface. This effect

<sup>\*</sup>Corresponding author: [zjudengjian@zju.edu.cn](mailto:zjudengjian@zju.edu.cn)

was initially identified by Doostmohammadi *et al.* [5]. By quantifying the additional drag caused by different mechanisms, Zhang *et al.* [7] found that the vorticity field contributes primarily to the drag enhancement, while the buoyancy of the lighter fluid plays a secondary role. A splitting procedure was proposed to decompose the force of a uniformly descending particle in a linearly stratified fluid. The force is divided into three components  $F_{\rho\rho}$ ,  $F_{\rho u}$ , and  $F_{\rho\omega}$ , corresponding respectively to the additional Archimedes buoyancy, the inertial force from the momentum flux, and the force caused by the baroclinic vorticity. Mandel *et al.* [21] studied the stratification drag acting on a rising droplet using experimental data and found that the ratio of the stratification drag to its homogeneous counterpart is scaled by  $\text{Fr}^{-0.89}\text{Re}^{-0.56}$ , agreeing well with the previous prediction of  $F_{\rho\omega} \sim \text{Fr}^{-1}\text{Re}^{-0.5}$  [7]. We note that the enhanced drag for a droplet is relatively smaller than that of a solid particle, due to the slip boundary on it [22].

Internal wave is another characteristic flow structure in a stratified fluid. For a particle moving vertically in a linearly stratified fluid, the far-field internal wave pattern can be predicted by a linear theory, proposed by Mowbray and Rarity [4], which has been validated by recent numerical and experimental studies [5,15]. The propagation of internal waves transfers momentum away from the source, i.e., the particle, and leads to an extra drag, referred to as wave resistance. However, the wave resistance is found to be significantly smaller than the inertial and viscous drags, unless when the stratification is strong ( $\text{Fr} \leq 3$ ) or as the Reynolds number is high [ $\text{Re} \geq O(10^3)$ ] [23].

The enhanced drag caused by the stratification effects delays the settling of the particle and yields a minimal velocity much lower than the local terminal velocity [9–11]. We believe that the ascending flows might be responsible for an intriguing bounce behavior of the particle settling through a density transition layer, in which the particle motion switches from falling to rising [24]. This phenomenon is surprisingly unique, since it occurs in the vicinity of a stratified density profile, in the complete absence of surface tension. It is easy to understand that the occurrence of bounce depends strongly on the relative density of the particle to its ambient fluid. In the previous experiments, the particles of different densities were tested, with only the lightest particle, whose density is very close to the bottom layer fluid, found to reverse its direction of motion [24]. Doostmohammadi and Ardekani [17] reported that an elongated particle levitates temporarily at a relatively high density jump between the top and bottom fluid layers.

More recently, Camassa *et al.* [25] conducted experiments of density triplets to ascertain the critical particle density at which the particle arrests, with given upper and lower density. They also performed a theoretical calculation exploring how the potential energy of the system under assumptions of potential flow provides a criterion predicting the critical sphere density for arrestment. Their theoretical prediction aligns closely with the experiments. It reveals that the available potential energy increases as the layer thickness decreases, suggesting that the critical particle density increases as the interface thickness decreases and approaches an upper bound for infinitely thin interfaces. Consequently, it can be inferred that the thicker transition layers are less capable of arresting

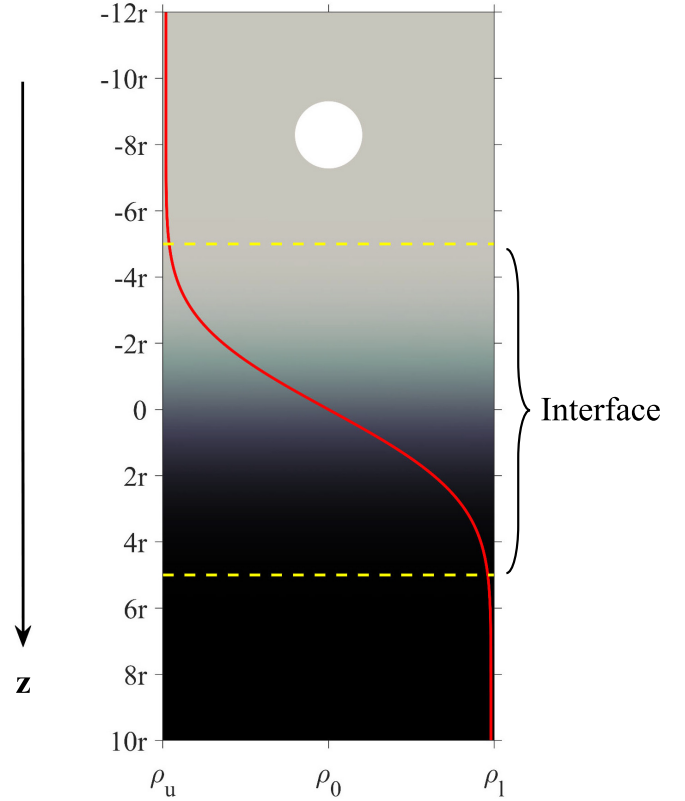


FIG. 1. The schematic of the numerical setup.

the particle. This trend has also been revealed in a linearly stratified fluid, in which the motions of particles and droplets were found to be altered from oscillation to unidirectional settling as the Froude number is increased, or equivalently by increasing the interface thickness if both the top and bottom layer densities are fixed [5,26].

From a contrasting perspective, it is intuitively postulated that a particle settling through a thin transition layer would exhibit a greater propensity for bouncing. To ascertain the veracity of this assertion, the present investigation employs numerical simulations. Particular emphasis is placed on examining the parameter ranges wherein distinct instances of bouncing can be observed. These include moderate Reynolds numbers for the upper-layer fluid, a comparably lower Reynolds number for the lower-layer fluid, and a particle with a slightly greater density than that of the lower-layer fluid.

The rest of this paper is organized as follows. The numerical method is briefly described in Sec. II. Numerical validation is demonstrated in Sec. III. The main results and discussions are presented in Sec. IV. We draw the conclusions in Sec. V.

## II. NUMERICAL METHOD

We study the gravitational settling of a spherical particle through a density interface, or a density transition layer, as illustrated in Fig. 1. The particle has a diameter  $D$  and a density  $\rho_p$ . The density interface has a thickness  $L$ , which is defined as the density transition region covering 98% of the density difference between the upper and lower layers. The

undisturbed density profile is specified as

$$\rho = \frac{\rho_u + \rho_l}{2} + \frac{\rho_u - \rho_l}{2} \text{erf}(\alpha z), \quad (1)$$

where  $\rho_u$  and  $\rho_l$  are, respectively, the upper- and lower-layer fluid density,  $z$  is the vertical position, with  $z = 0$  corresponding to the middle of the density transition layer,  $\alpha$  is a scaling factor, determining the thickness of the interface, and  $\text{erf}(x) = \frac{2}{\pi} \int_0^x e^{-t^2} dt$  is the error function.

The stratified fluid flow is governed by time-dependent incompressible Navier-Stokes equations. The continuity and the momentum equations are given as

$$\nabla \cdot \mathbf{u} = 0, \quad (2)$$

$$\rho \left( \frac{\partial \mathbf{u}}{\partial t} + \mathbf{u} \cdot \nabla \mathbf{u} \right) = -\nabla p + \mu \nabla^2 \mathbf{u} + \rho \mathbf{g}, \quad (3)$$

where  $\mathbf{u}$  is the velocity,  $p$  is the pressure,  $t$  is the transient time,  $\mu$  is the dynamic viscosity and  $\mathbf{g}$  is the gravitational acceleration, which has a nonzero component at  $z$  direction. Note that  $z$  is positive downward (Fig. 1). A transport equation for the solution of density field is introduced, expressed as

$$\frac{\partial \rho}{\partial t} + \mathbf{u} \cdot \nabla \rho = \kappa \nabla^2 \rho, \quad (4)$$

where  $\kappa$  is defined as  $\kappa = \nu/\text{Pr}$ . Corresponding to the salinity-induced stratification in water, we fix the Prandtl number at  $\text{Pr} = 700$ , with the kinematic viscosity of the fluid  $\nu = 1.38 \times 10^{-6} \text{m}^2/\text{s}$  and diffusivity  $\kappa = 1.97 \times 10^{-9} \text{m}^2/\text{s}$ . The Boussinesq approximation is applied to account for the stratification effect, where the density variation enters the momentum equation only through the buoyancy term. Division by the reference density in (3) yields

$$\frac{\partial \mathbf{u}}{\partial t} + \mathbf{u} \cdot \nabla \mathbf{u} = -\frac{1}{\rho_0} \nabla p + \frac{\rho}{\rho_0} \mathbf{g} + \nu \nabla^2 \mathbf{u}, \quad (5)$$

where  $\nu = \mu/\rho_0$  is the kinematic viscosity. Normalizing the lengths, velocities, time, pressure, and density by  $D$ ,  $U$ ,  $D/U$ ,  $\rho_0 U^2$ , and  $(\rho_l - \rho_u)D/L$  respectively, the governing equations can be expressed in nondimensional forms as follows:

$$\nabla \cdot \mathbf{u}' = 0, \quad (6)$$

$$\frac{\partial \rho'}{\partial t'} + \mathbf{u}' \cdot \nabla \rho' = \text{Pr}^{-1} \text{Re}^{-1} \nabla^2 \rho', \quad (7)$$

$$\frac{\partial \mathbf{u}'}{\partial t'} + \mathbf{u}' \cdot \nabla \mathbf{u}' = -\nabla p' - \text{Fr}^{-2} \rho' \mathbf{e}_z + \text{Re}^{-1} \nabla^2 \mathbf{u}'. \quad (8)$$

The governing equations are solved by a code based on the finite volume method [27]. The convection terms are discretized using the second-order upwind scheme, and the central differences scheme is used for the Laplacian terms. The time discretization scheme is the second-order implicit Euler. The pressure-velocity coupling is obtained using the pressure implicit with splitting of operators (PISO) scheme. At the particle surface, the velocity boundary condition is set as moving-wall velocity, and zero-gradient boundary conditions are set for the pressure and density. The top boundary has a fixed pressure  $p = 0$  and density  $\rho = \rho_u$ . The density at the bottom boundary is fixed to be  $\rho = \rho_l$ . For other boundaries, a fixed-flux condition is adopted for the pressure,

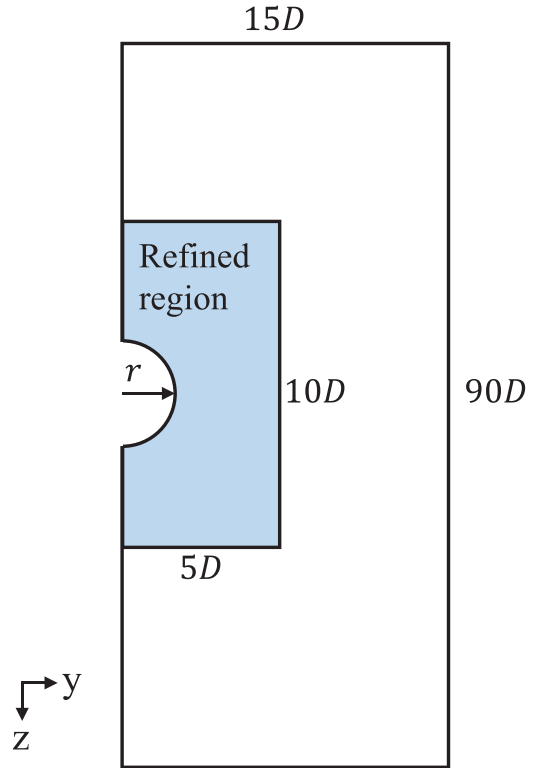


FIG. 2. The computational domain, with a region encompassing the particle marked for mesh refinement.

and a zero-gradient condition is specified for the velocity and density. The considered Reynolds numbers in the present work are in the range  $29 \leq \text{Re} \leq 259$ , which allows the usage of axisymmetry assumption. As reported previously that in a homogeneous fluid, the flow past a sphere is axisymmetric at  $\text{Re} < 200$  [28]. While, in a stratified fluid, the axisymmetric flow structure can retain at a Reynolds number up to 356 [5].

The vertical motion of the particle is determined by the total force acting on it using Newton's second law:

$$\rho_p \frac{1}{6} \pi D^3 \frac{d^2 z}{dt^2} = F_z, \quad (9)$$

where  $F_z$  is the vertical force on the particle, i.e., the gravity subtracting the hydrodynamic force. We solve (9) using the Newmark method [29]. The whole computational domain moves along with the particle, avoiding the problem of mesh deformation, as we adopted in our previous study [30].

### III. NUMERICAL VALIDATION

#### A. Mesh resolution test

In our numerical simulations, we employ axisymmetric assumption, rendering the geometry of our numerical model two dimensional, with the computational domain depicted in Fig. 2. The mesh is refined within a square region of length  $10D$  that encompasses the particle. Within this refined region, the mesh cell thickness increases at a fixed ratio from the particle's surface to the boundary. Our mesh-moving strategy requires the entire domain to move rigidly with the particle, causing the position of the density interface to vary relative

TABLE I. Detailed information of five different mesh resolutions used for the resolution test.

Mesh No.	First layer thickness	Total cell number
#1	0.0037 <i>D</i>	92680
#2	0.0028 <i>D</i>	166125
#3	0.0019 <i>D</i>	374821
#4	0.0016 <i>D</i>	537435
#5	0.0014 <i>D</i>	664500

to the mesh. To minimize numerical diffusion of the density interface, the cell height in the  $z$  direction remains constant outside the refined region.

To validate the mesh resolution, we conduct tests using five different mesh configurations for the case with the thinnest density interface  $L/D = 0.5$  and the highest upper Reynolds number  $Re_u = 259$ , which corresponds to the most pronounced stratification within our defined parameter range. The mesh details are presented in Table I. According to prior studies, the momentum and density boundary layer thickness can be estimated, respectively, by the following expressions [31]:

$$l_m \sim O\left(\frac{D}{\sqrt{Re}}\right) \quad (10)$$

and

$$l_d \sim O\left(\frac{D}{\sqrt{RePr}}\right). \quad (11)$$

With  $Pr = 700$  and  $Re_u = 259$ , these equations yield a minimum boundary thickness of  $l_m \sim 0.0621D$  and  $l_d \sim 0.0023D$  in our simulation, which aligns with our results. Figure 3 illustrates the differences in settling velocities between various mesh resolutions. We observe that the variations in these profiles become little as the first layer thickness is less than  $0.0023D$ , i.e., for the meshes #3, #4, and #5. Specifically, the difference in total velocity variation between mesh #5 and #4

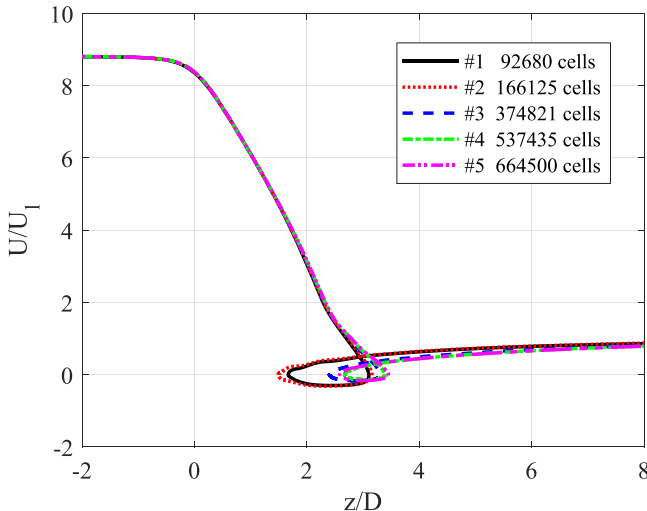


FIG. 3. Comparison of the settling velocities among different mesh resolutions at  $L/D = 0.5$  and  $Re_u = 259$ .

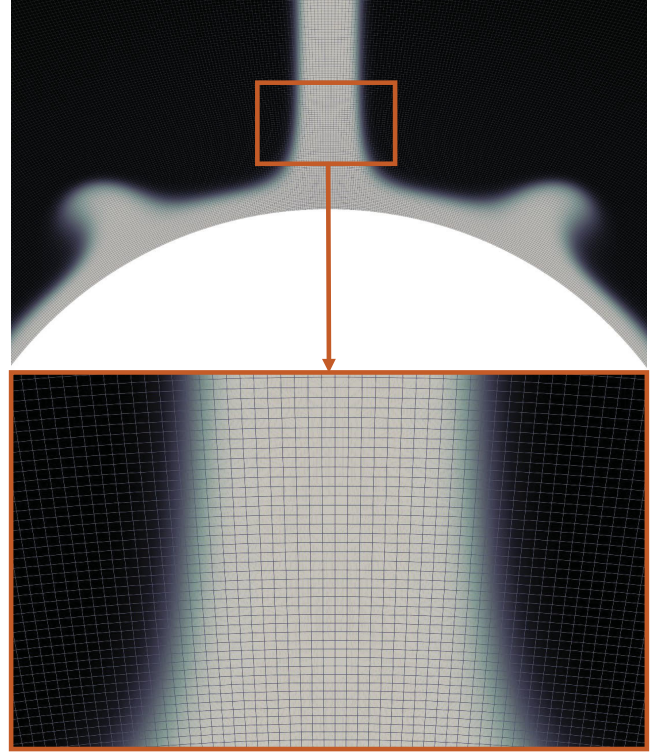


FIG. 4. A close-up view of the solved density field and the detailed cell distributions of mesh #5. This snapshot corresponds to the instant  $t' = 9.23$  at  $L/D = 0.5$  and  $Re_u = 259$ .

is less than 0.3%. We understand that it is not necessary to further increase the mesh resolution. In fact, when the minimal velocity serves as the criterion for identifying the rebound, even mesh #3 produces satisfactory results. Figure 4 provides a close-up view of the solved density field using mesh #5, confirming its capability to capture small structures around the particle surface, as well as the stretched thin tail along the central axis. Consequently, mesh #5 with 664 500 cells is chosen for the subsequent work.

### B. Validation of the Boussinesq approximation

To evaluate the validity of the Boussinesq approximation, we perform a series of numerical simulations wherein the Boussinesq approximation is not employed. Here, we present the results obtained at  $L/D = 0.5$  and  $Re_u = 259$ , in which the mesh resolutions have been tested. By comparing the results obtained using the Boussinesq approximation to those obtained without it, wherein the original equation (3) is solved, we observe a negligible quantitative disparity. The discrepancy in minimum velocities amounts to less than 1%, as illustrated in Fig. 5. The difference in flow structure induced by the Boussinesq approximation can be identified by comparing the baroclinic torque distribution, as depicted in Fig. 6. The original baroclinic torque  $\mathbf{T}_g = \nabla p \times \nabla(\frac{1}{\rho})$  (the left half in each panel) can be simplified as  $\mathbf{T}_g = \frac{1}{\rho_0} \nabla \rho \times \mathbf{g}$  (the right half in each panel) under the Boussinesq approximation [13]. A marginal deviation is evident only in the remote wake region, without exerting any significant influence on the settling dynamics of the particle.



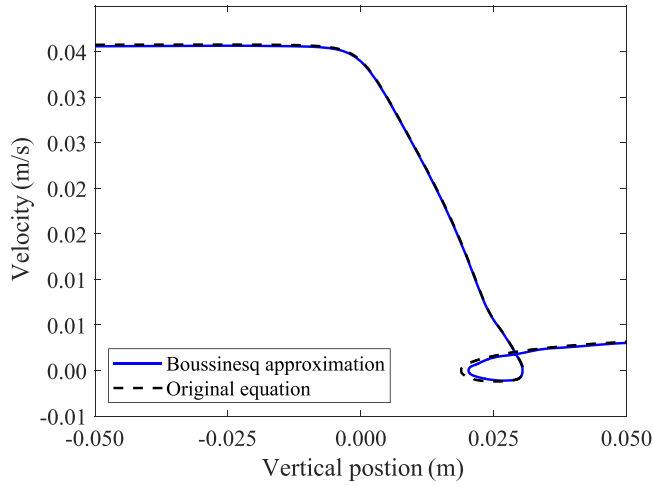


FIG. 5. The comparison of the evolution of the settling velocity with and without using the Boussinesq approximation, at  $L/D = 0.5$  and  $Re_u = 259$ . Note that both cases are simulated using mesh #5 with 664500 cells.

### C. Comparing with experimental results

The numerical method has been validated in our previous studies for a stratified flow past a cylinder [33] and a pitching foil [34,35]. Here, we validate the results for the gravitational settling of a particle in both homogeneous and stratified fluids. For a homogeneous fluid, the transient velocity of a settling particle with a terminal settling Reynolds number  $Re = 41$  is compared with the experimental measurements by Mordant and Pinton [32]. As shown in Fig. 7, the development of the simulated velocity agrees well with the measured data by Mordant and Pinton [32]. The difference in terminal velocities

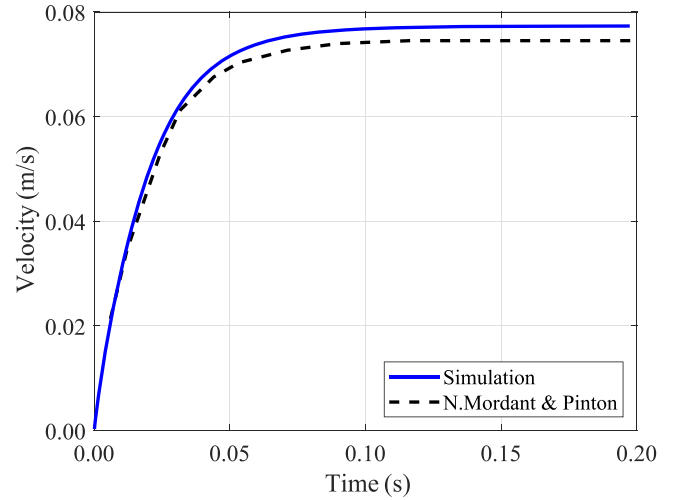


FIG. 7. Comparison with the experimental study [32] in the velocity profiles of a particle settling in a homogeneous fluid at  $Re = 41$ .

between the two results is less than 4%, indicating an accurate prediction by the present numerical solver.

Additionally, we have conducted experiments to validate the numerical method for stratified fluid. More details about the experimental setup can be found in Ref. [36]. A particle with a diameter  $D = 10.121$  mm and a density  $\rho_p = 1126.36$  kg/m<sup>3</sup> is released from a homogeneous layer with a density  $\rho_u = 1119.42$  kg/m<sup>3</sup>. After a period of time, the particle settles into a lower layer with a density  $\rho_l = 1125.90$  kg/m<sup>3</sup>, after passing through a density interface of thickness 2.78 cm. The particle experiences a bouncing motion in the lower layer after it passes the density interface. We set the simulation according to these properties in the experiment, except that a uniform viscosity is used for the whole domain in the simulation, while in the experiment the lower-layer fluid has a viscosity slightly higher than the upper fluid. The comparison of velocity profiles is presented in Fig. 8. The discrepancy between the two profiles stems from a slight variance in the lower-layer Reynolds numbers. The bouncing behavior is well captured in the simulation. The smaller bouncing distance in simulation is possibly caused by the smaller viscosity of fluid in the lower layer. The comparison of flow structure in the wake between simulations and experiments is presented in Fig. 9, suggesting a good agreement for the transient process of the dragging and rupture of upper fluid.

## IV. RESULTS

We consider a particle settling across a density interface from an upper light fluid layer to a lower dense fluid layer. The characterizing parameters include the upper-layer Reynolds number  $Re_u = U_u D / \nu$ , the lower-layer Reynolds number  $Re_l = U_l D / \nu$ , and the Froude number  $Fr = U_u / ND$ , where  $U_u$  and  $U_l$  are, respectively, the terminal velocities in the upper and lower homogeneous fluids,  $\nu$  is the kinematic viscosity of the fluid,  $D$  is the particle diameter,  $N$  is the

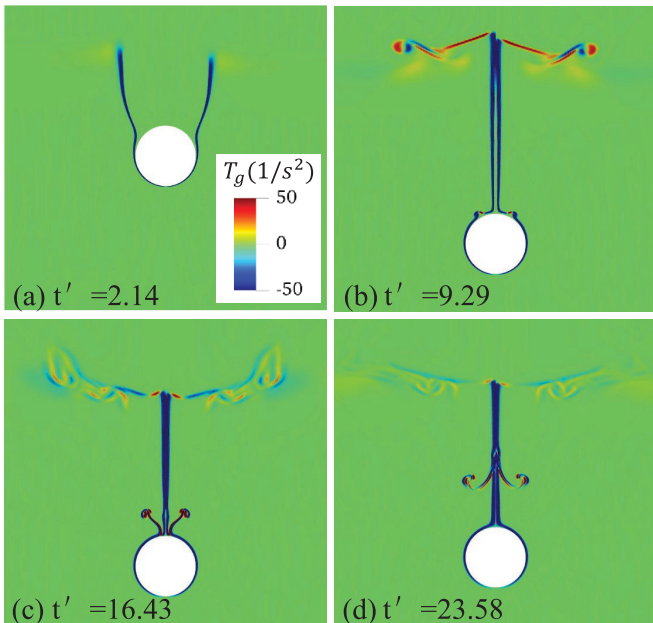


FIG. 6. The comparison of the baroclinic torque fields with (the right half in each panel) and without (the left half in each panel) using the Boussinesq approximation, at  $L/D = 0.5$  and  $Re_u = 259$ .

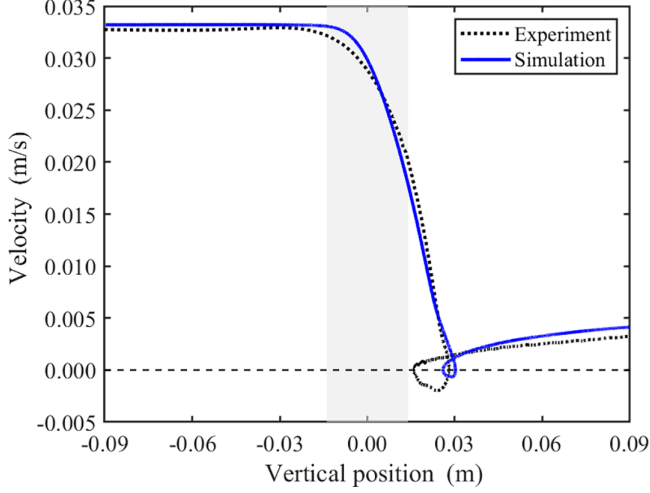


FIG. 8. Comparison with the experimental study [33] in the velocity profiles of a particle settling through a density interface with thickness  $L/D = 2.8$ . The nondimensional parameters are  $Re_u = 198$ ,  $Re_l = 20$  for experiment and  $Re_u = 198$ ,  $Re_l = 26$  for simulation (using mesh #5).

Brunt-Väisälä frequency defined as

$$N = \sqrt{\frac{g}{\rho_0} \frac{\rho_l - \rho_u}{L}}, \quad (12)$$

where  $\rho_0 = (\rho_u + \rho_l)/2$  is the reference density,  $L$  is the thickness of the density transition layer, covering 98% of the density variation.

In our simulations, we fix the densities of the lower-layer fluid and the particle, with a density ratio of  $\eta_l = \rho_l/\rho_p = 0.9997$ , which yields  $Re_l = 29$ . Four upper density ratios are considered, varying from  $\eta_u = \rho_u/\rho_p = 0.9938$ – $0.9991$ , resulting in  $Re_u = 259 \sim 69$ . For each combination of upper

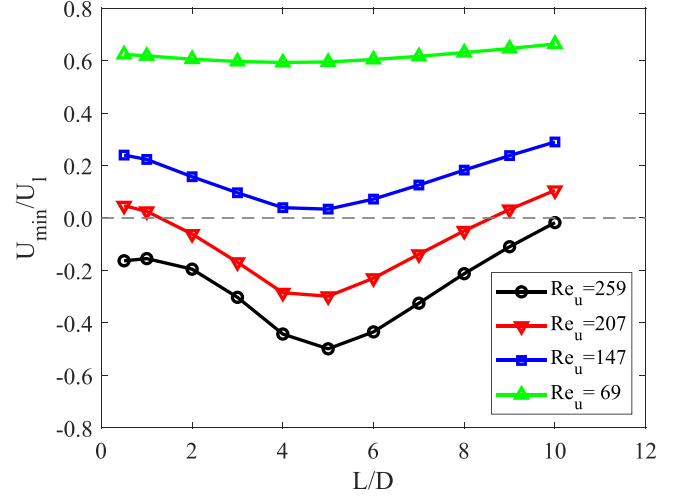


FIG. 10. The variation of nondimensional minimal velocity with the interface thickness for four different upper layer Reynolds numbers  $Re_u = 259, 207, 147$ , and  $69$ .

and lower density ratios, the interface thickness is varied in the range of  $L/D = 0.5 \sim 10$ . Due to an error-function-type density transition layer we considered, the variation of  $L/D$  simultaneously changes the Froude number, resulting in a range of  $0.86 \leq Fr \leq 4.66$ . The transient time is counted from the instant when the centroid of the particle moves to the middle of the density interface ( $z = 0$ ), and normalized by  $\tau = D/U_u$ . For each simulation, the particle is set to settle in the upper layer for  $10\tau$  before reaching the upper bound of the density interface, to ensure that a steady-state velocity is reached. It is important to mention that all simulations are performed using mesh #5 with 664 500 cells, of which the resolution has been tested in Sec. III A.

#### A. Settling dynamics of the particle

First, we investigate the effects of interface thickness on the temporal bouncing behavior of the settling particle. Figure 10 shows the variation of the minimum velocity of the particle, normalized by its terminal velocity in the homogeneous lower layer, over the interface thickness at the range of  $L/D = 0.5 \sim 10$ . A negative value of  $U_{\min}/U_l$  represents the occurrence of bouncing behavior, and the positive  $U_{\min}/U_l$  corresponds to a unidirectional settling. We examine four different upper density ratios  $\eta_u = 0.9938, 0.9956, 0.9973$ , and  $0.9991$ , corresponding to  $Re_u = 259, 207, 147$ , and  $69$ , respectively. Clearly, the minimal velocity increases with decreasing upper Reynolds number (equivalently the increasing upper density ratio). At a low upper Reynolds number,  $Re_u = 69$ , the minimal velocity is approximately constant and positive despite the variation of  $L/D$ . While at the highest upper Reynolds number,  $Re_u = 259$ , the minimal velocities are negative for all interface thicknesses, suggesting the occurrence of bounce. The restraining effect by the density interface on the settling particle is significant. The minimal velocity is approximately 60% of the lower-layer terminal velocity, even for the case of  $Re_u = 69$  with the slightest influence. The interface thickness also plays an important role in determining the particle behavior. As the thickness increases from  $L/D = 0.5$ – $10$ , the

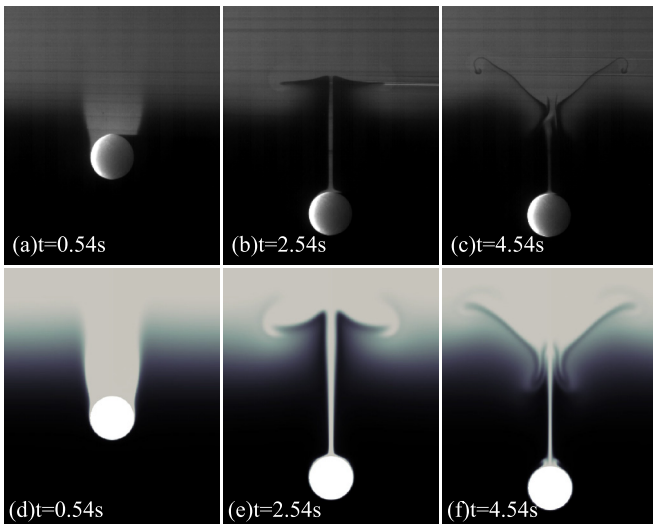


FIG. 9. Comparison with the experimental study [33] in the transient flow structure between experiment (a)–(c) and simulation (d)–(f) of a particle settling through a density interface with thickness  $L/D = 2.8$ . The nondimensional parameters are  $Re_u = 198$ ,  $Re_l = 20$  for experiment and  $Re_u = 198$ ,  $Re_l = 26$  for simulation.

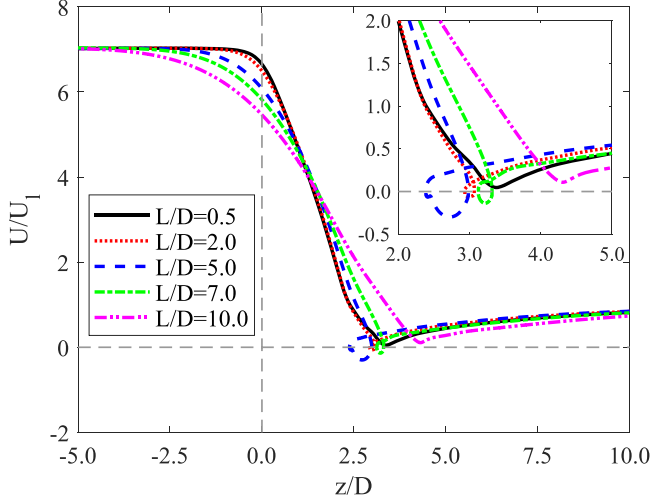


FIG. 11. The velocity profiles of particle settling through different interface thicknesses at  $Re_u = 207$ .

minimal velocity shows a nonmonotonic trend with a global minimum reached around  $L/D = 5.0$ , where the particle is most likely to bounce. As the interface becomes thinner or thicker, the particle tends to settle unidirectionally.

We note that the interface thickness enters the governing equation from the Froude number. The second term of the nondimensional momentum equation (8) can be written as

$$-\text{Fr}^{-2} \rho' e_z = \frac{U^2 \rho_0}{Dg(\rho_l - \rho_u)} \frac{L}{D} \rho' e_z. \quad (13)$$

The nonmonotonic trend of the particle behavior also reveals the effects of the Froude number.

In Fig. 10, we pay special attention to  $Re_u = 207$ , where the particle behaves differently as the interface thickness varies. The particle bounces for  $2 \leq L/D \leq 8$ , while it settles unidirectionally for  $L/D \leq 1$  and  $L/D \geq 9$ . We plot the velocity profiles in Fig. 11. The velocity is initially constant in the upper layer, and decreases rapidly after the particle enters the interface. The minimal velocity is reached at  $z/D = 2.5 \sim 5$  depending on the interface thickness. Finally, after the deceleration, the particle recovers slowly to the lower terminal velocity. As expected, a thinner interface leads to a steeper decline of the velocity, especially after the particle passes the middle of the interface ( $z/D = 0$ ). However, this trend breaks as the particle descends to approximately  $z/D = 2.5$ . The settling velocity at the thin interfaces  $L/D = 0.5$  and  $L/D = 2.0$  gradually exceeds that of  $L/D = 5.0$  and reaches a higher minimal velocity. Moreover, the velocity profile of  $L/D = 0.5$  and  $L/D = 2.0$  almost overlaps at the interface region, although their interface thicknesses differ remarkably.

In addition, we plot the time-dependent acceleration of the particle at  $L/D = 0.5, 5.0$ , and  $10.0$  in Fig. 12 for  $Re_u = 207$ . Note that  $t' = 0$  corresponds to the instant when the particle is crossing the middle of the transition layer. Clearly, the presence of the density interface increases significantly the drag on the particle. For the thinner interface, i.e.,  $L/D = 0.5$ , the deceleration is stronger and meanwhile it decays faster. At the beginning and end of the settling, the thicker interface provides a stronger deceleration.

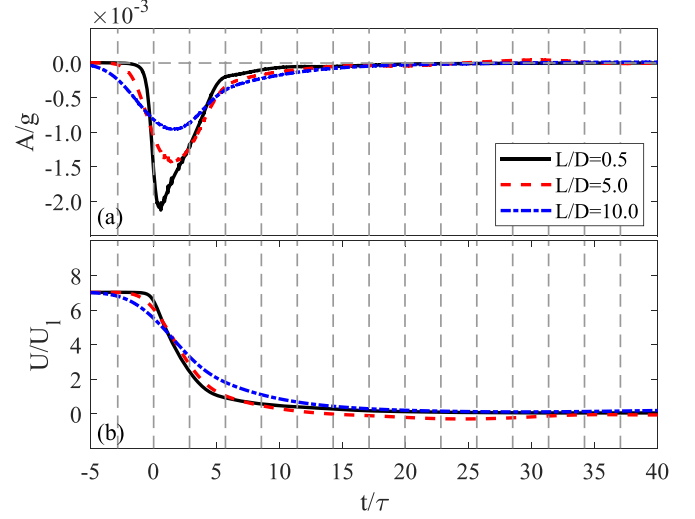


FIG. 12. Time evolution of the (a) acceleration and (b) velocity of particle at different interface thicknesses at  $Re_u = 207$ . Here, the time has been scaled by  $\tau = D/U_u$  the particle acceleration has been scaled by the gravity acceleration  $g$ .

## B. Flow structure and wake pattern

In this section, we detail the nontrivial flow structures as the particle settles across the interfaces with different thicknesses. The transient flow fields at different instants corresponding to the vertical dashed lines in Fig. 12 are shown in Figs. 13–15. The velocities of the particle are noted in these figures. Initially, the interface is deformed by the penetrating particle. A drift of light fluid from the upper layer is attached at the rear of the particle [see Figs. 13–15, panel (c)]. The dragged light fluid quickly detaches from the particle and restores to the upper layer under the buoyancy effect [so-called the first detachment, see Figs. 13–15, panel (d)]. For a thinner interface, the light fluid is dragged deeper relative to the interface. For example, as seen in Fig. 13(c) for  $L/D = 0.5$ , the drift fluid is dragged into the lower layer far below the interface before it detaches. In contrast, for the thicker interfaces,  $L/D = 5.0$  and  $10.0$ , the detachment nearly completes before the particle leaves the transition layer, as seen in Figs. 14(e) and 15(e), where an additional small, but non-negligible, amount of upper fluid remains attached on the rear surface of the particle, which has also been observed in the previous experiments [24,33]. For  $L/D = 0.5$ , a distinct, small roll-up structure manifests around the particle surface after the initial detachment [refer to Fig. 13(h)]. This phenomenon is referred to as the secondary detachment, characterized by the separation of the boundary layer flow and the detachment of the still-present lighter fluid. Notably, this roll-up structure is absent at  $L/D = 5.0$  and  $L/D = 10.0$ . Evidently, the process of secondary detachment is influenced by the thickness of the interface, as depicted in Fig. 16. For  $L/D \leq 3.0$ , the remaining lighter fluid detaches at an angle from the central axis. As the interface thickness increases, the detachment point gradually shifts towards the rear stagnation point. At intermediate interface thicknesses, such as  $L/D = 4.0$  and  $L/D = 5.0$ , the detached fluid converges but ascends towards the upper layer along the central axis. In the

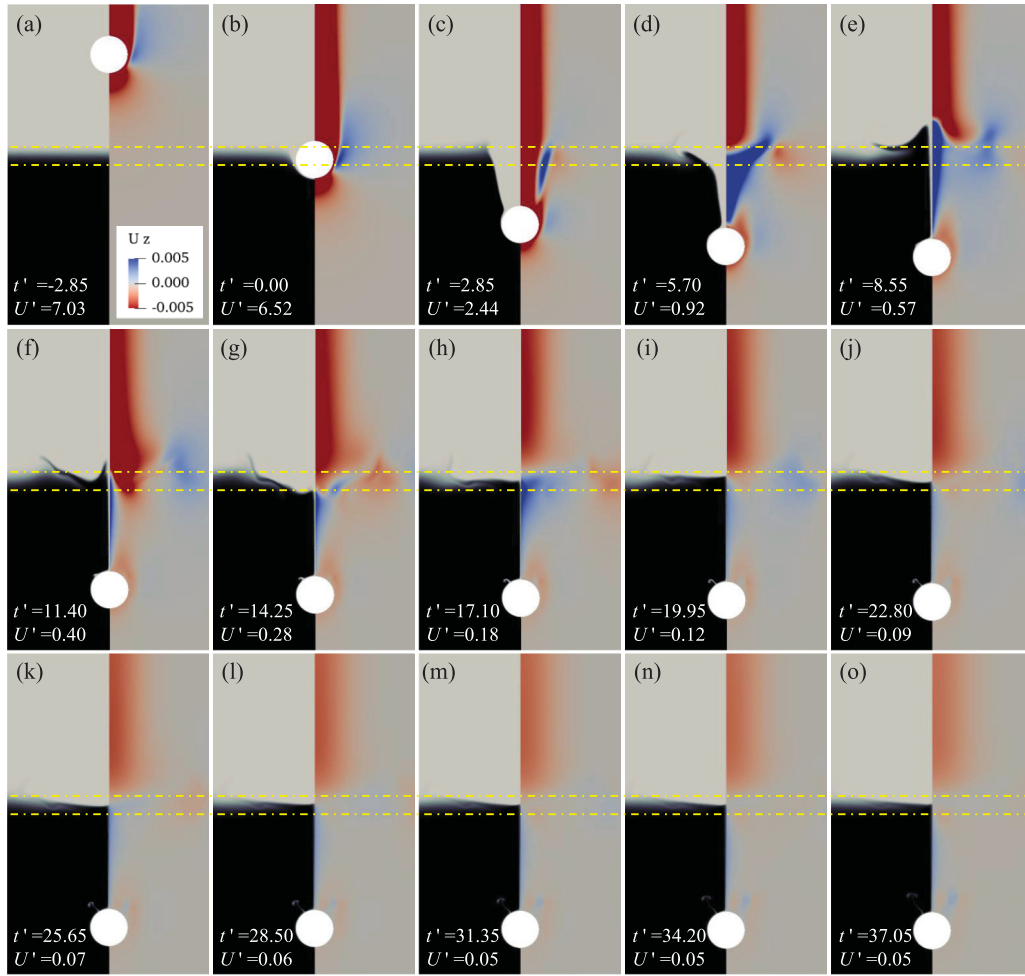


FIG. 13. A sequence of images, showing the settling of a particle passing through a density transition layer with thickness  $L/D = 0.5$  at  $Re_d = 207$ . For each panel, the left half shows the contours of the density field, and the right half shows that of the vertical velocity component. The interface bounds are marked by two dashed lines.

case of a thicker interface, such as  $L/D = 10.0$ , the remaining lighter fluid returns to the upper layer continuously without accumulating at the particle surface.

The detachment process can be characterized by tracking the movement of the attachment point of the drifting fluid. Its position is represented by the separation angle, defined as the angle between the rear stagnation point and the separation point (refer to the inset of Fig. 17). The quantified results are presented in Fig. 17. Consistent with the detachment progression of the caudal fluid, the separation angle diminishes over time for all interface thicknesses.

For the thinner interface, the angle decreases more rapidly, indicative of a swifter detachment owing to the larger buoyancy force experienced by the trailing fluid. We observe that, for intermediate interface thicknesses, the separation angle exhibits a nonmonotonic behavior and reaches a local maximum (see  $L/D = 5.0$  and  $7.0$  in Fig. 17). This local maximum is correlated with the accumulation of the remaining lighter fluid, as depicted in Fig. 16(f). The temporal variation of the secondary detachment angle for  $L/D \leq 3.0$  is illustrated in Fig. 18. The remaining lighter fluid detaches from approximately  $\theta_d \approx 50^\circ$  and moves towards the rear stagnation point. However, it does not reach the central axis during the entire

detachment process, thus not affecting the monotonic trend of  $\theta_d$ .

Examining the velocity fields, we find an upward flow, in an opposite direction to the particle, of the entrained fluid, initially observed at the edge of the drift [see the deep blue region of Fig. 13(c)], which spreads quickly to the central axis [see Fig. 13(d)]. This upward jet originates from the potential energy, generated as the entrained fluid suddenly becomes less dense than the surrounding fluid the particle is moving in. This potential energy tends to be restored by the entrained fluid moving back into the top layer, which necessarily, through viscous coupling, exerts an additional upward force upon the particle. Another notable difference is in the perturbed interface after completing the first detachment, i.e., from  $t' = 11.40$  [see panel (f) in Figs. 13–15]. For the thinnest interface,  $L/D = 0.5$ , a splash phenomenon is spotted, resembling that which occurs for an object dropping on a water surface. The interface restores quiet after the perturbation propagates far away in the form of interval waves. Instead, for  $L/D = 5.0$  and  $10.0$ , a vortex ring forms around the upper bound of the transition layer, as presented in Fig. 19. We note that in a similar parametric range, such a caudal jet flow has also been observed in a linearly stratified fluid, with variations of the



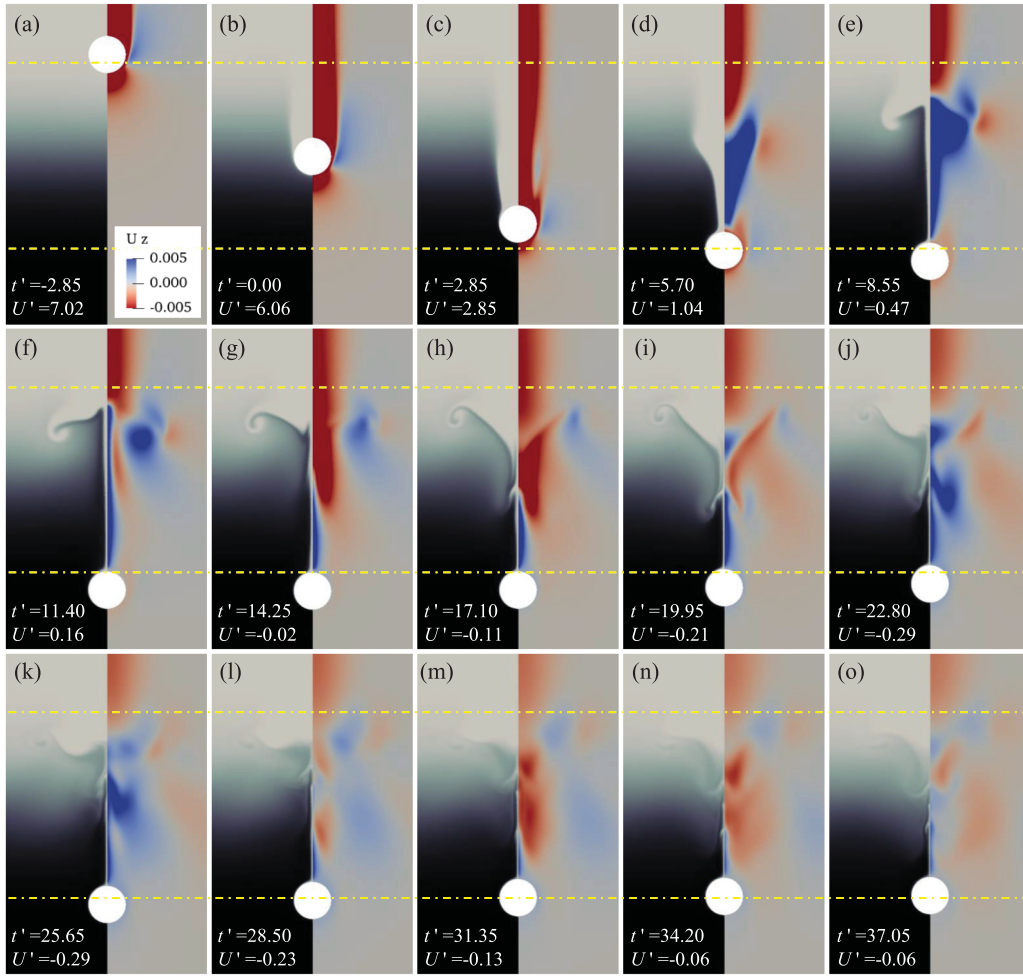


FIG. 14. A sequence of images, showing the settling of a particle passing through a density transition layer with thickness  $L/D = 5.0$  at  $Re_u = 207$ . For each panel, the left half shows the contours of the density field, and the right half shows that of the vertical velocity component. The interface bounds are marked by two dashed lines.

relevant flow structures reported [2]. However, they did not report the vortex ring.

After the first detachment, the drift shrinks horizontally and elongates vertically, reducing to a thin vertical column, or a filament. The light fluid within the vertical column restores slowly to the upper layer and diffuses with the ambient dense fluid. We find that there is more upper fluid remaining within the vertical column for the thicker interfaces, which can be explained by the fact that the particle settles a longer distance within the transition layer, resulting in less diffusion from the dragged fluid to its surrounding dense fluid.

An additional observation worth noting is the presence of a bell-shaped knot structure along the central vertical column in Fig. 14(h) for  $L/D = 5.0$ , as well as in Fig. 15(k) for  $L/D = 10.0$ . This bell-shaped jet structure bears resemblance to similar structures reported in prior studies investigating linear stratified fluids through both experimental and simulation approaches. These studies have attributed the occurrence of such structures to the influence of internal waves [2,15].

### C. Drag enhancement mechanisms

It is easy to understand that the particle exhibits no bounce phenomenon for the very thick interfaces as we fix the density

triplets ( $\rho_u$ ,  $\rho_l$ ,  $\rho_p$ ). As seen clearly from the right branch, i.e.,  $L/D > 5$ , in Fig. 10, the minimum velocity increases as the interface becomes thicker, with a tendency to inhibit the bounce. In other words, the stronger stratification is more pronounced to reverse the particle's direction of motion. However, on the other hand, the minimum velocity decreases as the interface becomes thicker for  $L/D < 5$ , which deviates from our intuitive understanding and requires extra explanation. In this section, we aim to get further insight into this nontrivial phenomenon.

The analysis of the bouncing mechanism has been conducted in our previous study [33] through a force decomposition procedure. This analysis reveals that the increased drag experienced by the particle is primarily attributed to the buoyancy effects of the attached lighter fluid during the early stage before the first detachment. Subsequently, the specific flow structure predominantly contributes to the drag (see Fig. 11 in Ref. [33]).

Based on the bouncing mechanism, we first compare the effects of attached lighter fluid. We calculate the force component,  $F_b$ , induced by the hydrostatic pressure, or the buoyancy force induced by the nonuniformly distributed density. Figure 20 illustrates its variation for different interface

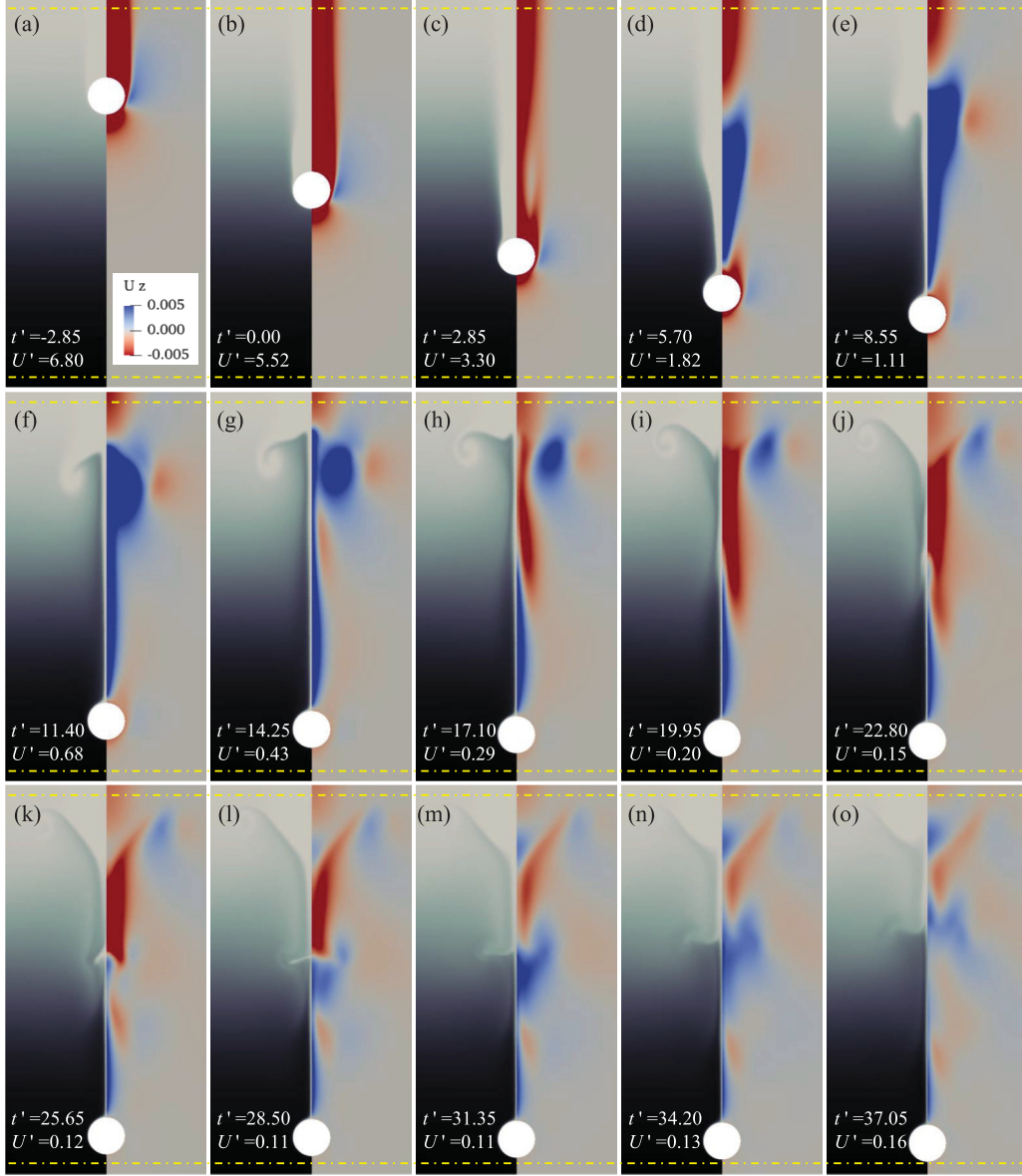


FIG. 15. A sequence of images, showing the settling of a particle passing through a density transition layer with thickness  $L/D = 10.0$  at  $Re_u = 207$ . For each panel, the left half shows the contours of the density field, and the right half shows that of the vertical velocity component. The interface bounds are marked by two dashed lines.

thicknesses. For  $L/D = 0.5$  and  $L/D = 5.0$ , it exhibits a nonmonotonic behavior, reaching its maximum value that surpasses the gravitational force acting on the particle. It is crucial to note that the density of the fluid is consistently lower than that of the particle. This peak in  $F_b$  is a consequence of the attachment of the trailing lighter fluid, commonly known as the drift, which imparts additional buoyancy to the particle. For thicker interface thicknesses, the buoyancy decreases monotonously once the particle enters the interface. In contrast, for  $L/D = 0.5$ ,  $F_b$  diminishes more rapidly, becoming smaller than that of  $L/D = 5.0$  at  $z/D = 2.2$ , as indicated in Fig. 20.

The magnitude of  $F_b$  is influenced by both the volume of the drift fluid and the density difference between the drift fluid and its ambient fluid [6, 10]. To investigate this relationship,

we plot the volume of the drift fluid, denoted as  $V_d$ , as a function of vertical position in Fig. 21.  $V_d$  is defined as the volume enclosed by the distorted isopycnal of  $\rho_0 = (\rho_u + \rho_l)/2$ , the particle surface, and the undisturbed interface (as illustrated in the schematic diagram in Fig. 21).

As the interface thickness decreases, a larger volume of light fluid becomes attached to the particle. This trend is consistent with the theoretical calculation conducted by Camassa *et al.* [25], which reveals that the potential energy (directly related to the drift volume  $V_d$ ) increases with decreasing interface thickness. Simultaneously, the density difference between the drift fluid and its ambient fluid increases. For instance, at  $z/D = 2.0$ , the particle and drift fluid penetrate the lower layer for the thin interface cases ( $L/D \leq 4.0$ ), resulting in a substantial density difference  $\Delta\rho = \rho_l - \rho_u$ . Conversely,

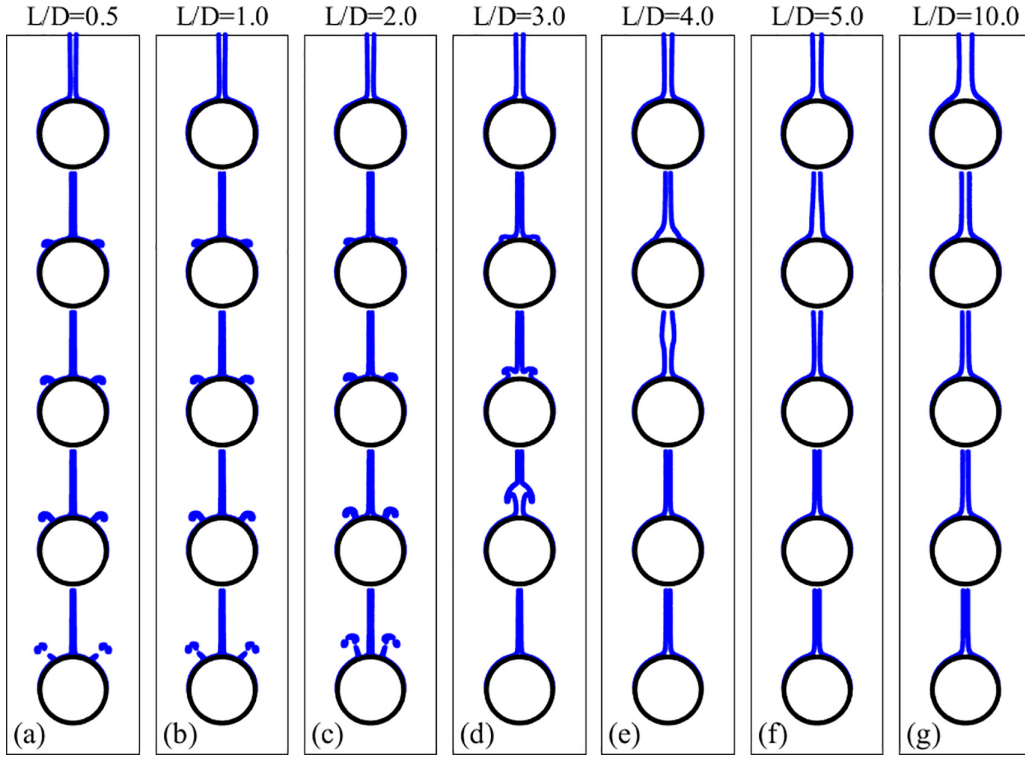


FIG. 16. The shapes of the isopycnal of  $\rho_0 = (\rho_u + \rho_l)/2$  at the time instants  $t' = 8.55, 14.25, 17.10, 19.95, 25.65$  from top to bottom.

for thicker interfaces ( $L/D \geq 5.0$ ), the position  $z/D = 2.0$  lies within the density transition layer, leading to a smaller density difference.

Consequently, at a thinner interface, the drift fluid contributes more buoyancy to the particle, leading to a larger value of  $F_b$ . The subsequent decrease in  $F_b$  is attributed to the detachment of the drifted fluid. The detachment process occurs more rapidly at thinner interfaces, as evidenced by the more pronounced decrease in  $V_d$  shown in Fig. 21. Notably, the vertical position at which  $V_d$  for  $L/D = 5.0$  exceeds that of

$L/D = 0.5$  is approximately  $z/D = 2.2$ , corresponding precisely to the transition point observed for  $F_b$  in Fig. 20.

The specific flow structure, such as baroclinic vorticity [5,7], and the upward jet [1,33], also play a significant role in the enhancement of drag. In Figs. 19(a) and 19(b), we observe that the baroclinic vorticity (blue region in the right panel) is notably stronger at  $L/D = 5.0$  compared to  $L/D = 0.5$  near the rear stagnation point, which leads to an increased shear rate and, consequently, greater stratification drag. Additionally, we propose that the secondary

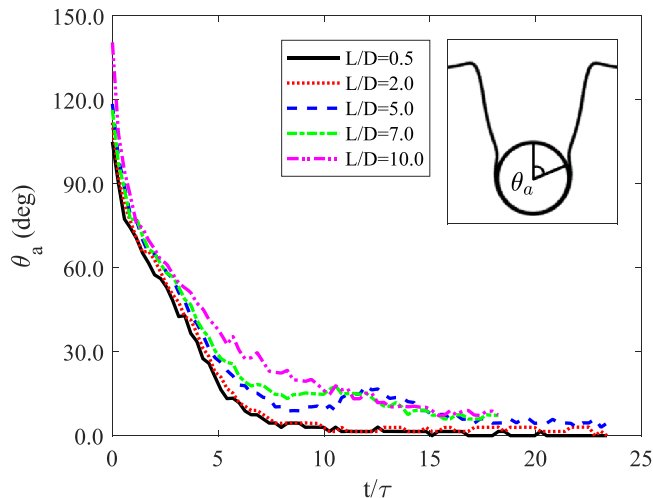


FIG. 17. The variations of separation angle  $\theta_a$  over time for different values of interface thickness.

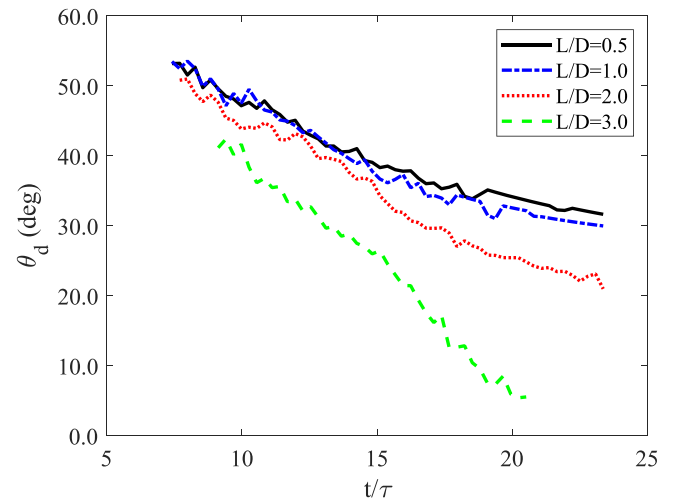


FIG. 18. The temporal variation of the secondary detachment angle  $\theta_d$  at different values of interface thickness.

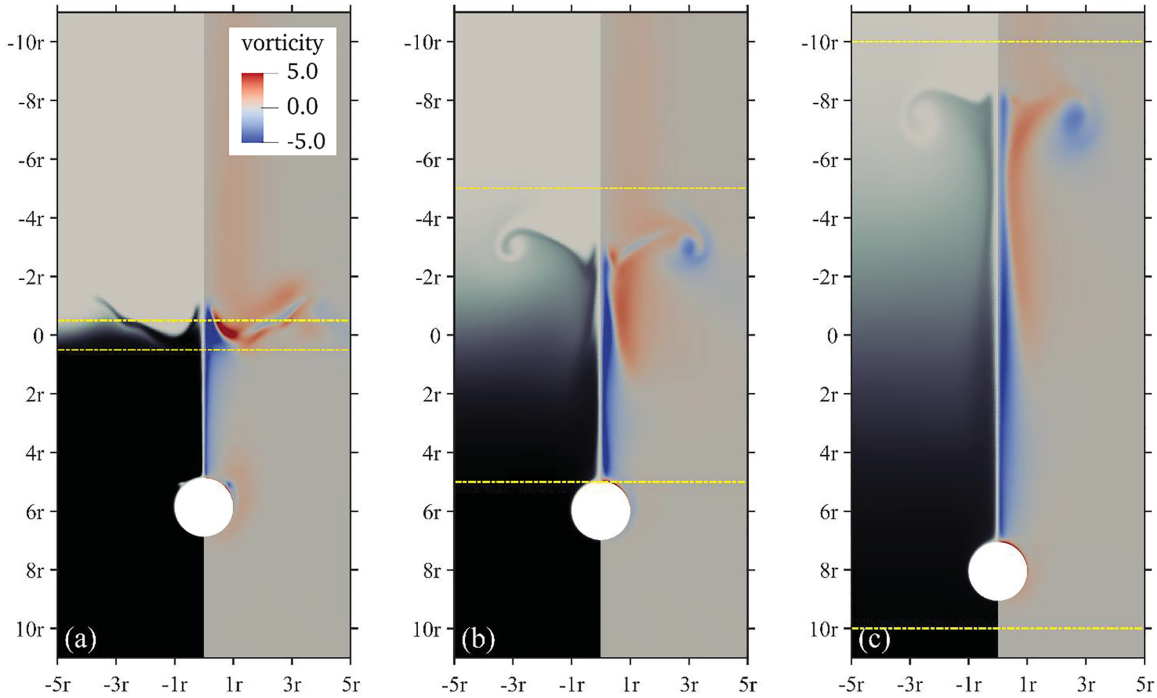


FIG. 19. A comparison of the vortex structure between different interface thicknesses for (a)  $L/D = 0.5$ ,  $t' = 11.40$ , (b)  $L/D = 5.0$ ,  $t' = 14.25$ , (c)  $L/D = 10.0$ ,  $t' = 17.10$  at  $Re_u = 207$ . The left half shows the contour of the density field, and the right half shows the vorticity field. The interface bounds are noted by the yellow dashed lines.

detachment also contributes to the higher minimal velocity at a thinner interface. On the one hand, the secondary detachment reduces the extra buoyant force generated by the lighter fluid. On the other hand, we observe that the secondary detachment suppresses the formation of a secondary jet. In Fig. 22, we show the time-evolved vertical velocities along the central axis for  $L/D = 0.5$ ,  $5.0$ , and  $10.0$ . Clearly seen is that the buoyant jet (deep blue region) emerges at a similar time instant around  $t' = 5-10$ , while it persists for a longer duration as the interface is thicker. For  $L/D = 5.0$ , a

secondary jet appears after the first jet vanishes. As depicted in Fig. 16(e), after the drift fluid detaches, the light fluid remaining at the particle surface coalesces and rises to the upper layer from the central axis, explaining the formation of the secondary jet. The rear jet exerts a lifting effect on the particle. At the same instant when the secondary jet is formed, the particle reverses its moving direction. However, at  $L/D = 0.5$ , the secondary jet is not detected as the remaining fluid detaches from the particle at an angle relative to the central axis.

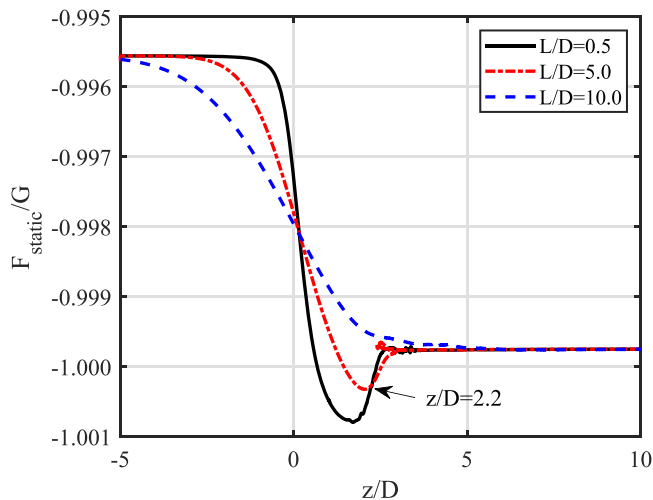


FIG. 20. The force component,  $F_b$ , induced by the hydrostatic pressure, normalized by its gravity,  $G$ , versus the vertical position for different values of density thickness.

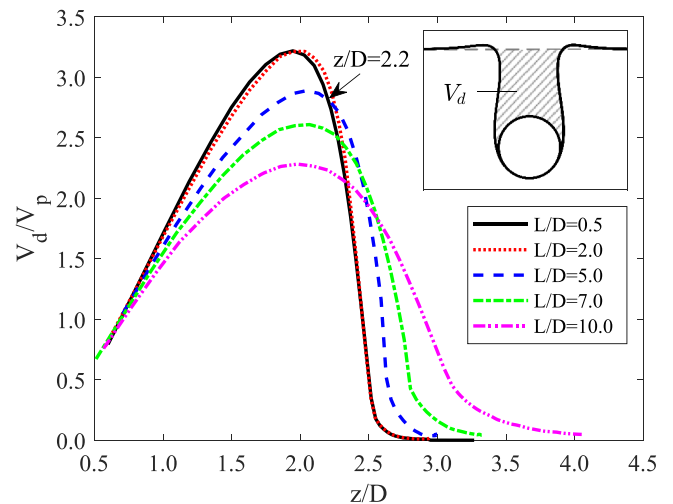


FIG. 21. The drifted fluid volume  $V_d$ , normalized by the volume of the particle  $V_p$ , versus the vertical position at different values of interface thickness.



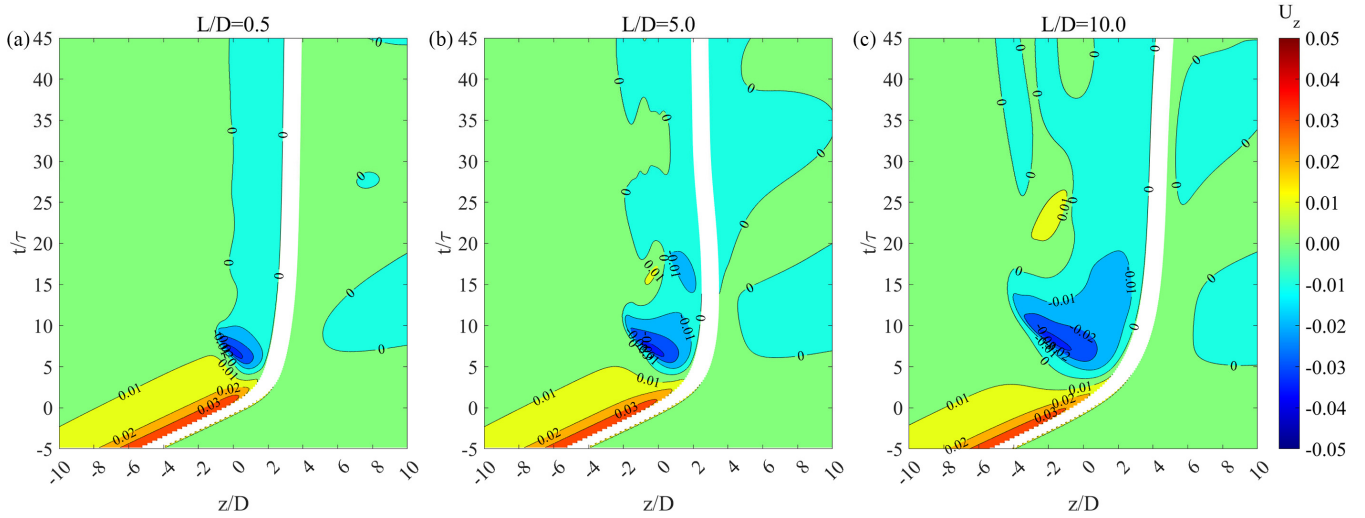


FIG. 22. The temporal development of the vertical velocity  $U_z$  along the central axis for (a)  $L/D = 0.5$ , (b)  $L/D = 5.0$ , and (c)  $L/D = 10.0$ . The white blank region is where the particle is located.

## V. CONCLUSIONS

We conduct numerical simulations to investigate the gravitational settling of a particle through a density transition layer, or interface, considering different interface thicknesses. The simulations are carried out using the Boussinesq approximation, allowing us to explore the effects of interface thickness on the bouncing behavior of the particle.

In our simulations, we keep the lower density ratio fixed at  $\rho_l/\rho_p = 0.9997$ , resulting in a lower Reynolds number of  $Re_l = 29$ . We vary the upper density ratios from  $\rho_u/\rho_p = 0.9938$  to  $0.9991$ , corresponding to a range of upper Reynolds numbers between  $Re_u = 259$  and  $69$ . We specifically examine interface thicknesses ranging from  $L/D = 0.5$ – $10$ , where  $L$  represents the interface thickness and  $D$  denotes the characteristic size of the particle.

Our results reveal a nonmonotonic variation in the minimal velocity of the particle as the interface thickness increased from  $L/D = 0.5$ – $10.0$ . This indicates that the bouncing motion of the particle is inhibited at both very thin and very thick interfaces. We particularly focus on understanding the inhibition of bouncing motion at very thin interfaces, which contradicts the intuitive understanding that a stronger stratification leads to a more pronounced velocity reduction. The observed nonmonotonic bounce behavior, dependent on the layer thickness, is attributed to flow instabilities that result in the shedding of drift fluid. We notice an increase in drift volumes as the layer thickness decreases, a trend akin to that reported in Ref. [25], but we see that additional shedding instabilities occur for the particle. Such instabilities were not

considered in Ref. [25], as their experiments were regulated to  $L/D > 2$ .

We propose that this inhibition can be attributed to two underlying mechanisms. First, as the interface becomes thinner, the lighter fluid that drifts along with the particle detaches more rapidly, resulting in a swift decrease in buoyancy. This reduction in buoyancy hinders the bouncing motion of the particle. Second, after the drift fluid detaches, there remains a small but significant amount of upper fluid at the particle surface. For very thin interfaces ( $L/D = 0.5$ – $2.0$ ), this remaining lighter fluid congregates and undergoes a secondary detachment from the particle. This detachment leads to a loss of light fluid, which, on one hand, reduces the drag force caused by buoyancy. On the other hand, the detached fluid deviates from the central axis, contributing less to the drag induced by the jet flow compared to cases with moderate interface thickness ( $L/D \approx 5.0$ ). In those cases, the remaining light fluid returns to the upper layer along the central axis, forming a secondary jet that enhances the jet-induced drag force.

We note that the obtained conclusions are limited to the current parametric range, for example, the lower limit we choose for the interface thickness is  $L/D = 0.5$ , to ensure the validity of the Boussinesq approximation. It will be of interest to investigate on the even thinner transition layer.

## ACKNOWLEDGMENTS

This research has been supported by the National Natural Science Foundation of China (Grant No. 92252102).

- [1] C. R. Torres, H. Hanazaki, J. Ochoa, J. Castillo, and M. Van Woert, Flow past a sphere moving vertically in a stratified diffusive fluid, *J. Fluid Mech.* **417**, 211 (2000).
- [2] H. Hanazaki, K. Kashimoto, and T. Okamura, Jets generated by a sphere moving vertically in a stratified fluid, *J. Fluid Mech.* **638**, 173 (2009).

- [3] H. Hanazaki, S. Nakamura, and H. Yoshikawa, Numerical simulation of jets generated by a sphere moving vertically in a stratified fluid, *J. Fluid Mech.* **765**, 424 (2015).
- [4] D. Mowbray and B. Rarity, The internal wave pattern produced by a sphere moving vertically in a density stratified liquid, *J. Fluid Mech.* **30**, 489 (1967).

- [5] A. Doostmohammadi, S. Dabiri, and A. M. Ardekani, A numerical study of the dynamics of a particle settling at moderate Reynolds numbers in a linearly stratified fluid, *J. Fluid Mech.* **750**, 5 (2014).
- [6] K. Y. Yick, C. R. Torres, T. Peacock, and R. Stocker, Enhanced drag of a sphere settling in a stratified fluid at small Reynolds numbers, *J. Fluid Mech.* **632**, 49 (2009).
- [7] J. Zhang, M. J. Mercier, and J. Magnaudet, Core mechanisms of drag enhancement on bodies settling in a stratified fluid, *J. Fluid Mech.* **875**, 622 (2019).
- [8] R. Camassa, C. Falcon, J. Lin, R. M. McLaughlin, and R. Parker, Prolonged residence times for particles settling through stratified miscible fluids in the stokes regime, *Phys. Fluids* **21**, 031702 (2009).
- [9] R. Camassa, C. Falcon, J. Lin, R. M. McLaughlin, and N. Mykins, A first-principle predictive theory for a sphere falling through sharply stratified fluid at low Reynolds number, *J. Fluid Mech.* **664**, 436 (2010).
- [10] A. N. Srdić-Mitrović, N. A. Mohamed, and H. E. S. Fernando, Gravitational settling of particles through density interfaces, *J. Fluid Mech.* **381**, 175 (1999).
- [11] L. Verso, M. van Reeuwijk, and A. Liberzon, Transient stratification force on particles crossing a density interface, *Int. J. Multiphase Flow* **121**, 103109 (2019).
- [12] J. Magnaudet and M. J. Mercier, Particles, drops, and bubbles moving across sharp interfaces and stratified layers, *Annu. Rev. Fluid Mech.* **52**, 61 (2020).
- [13] R. V. More and A. M. Ardekani, Motion in stratified fluids, *Annu. Rev. Fluid Mech.* **55**, 157 (2023).
- [14] A. M. Ardekani and R. Stocker, Stratlets: Low Reynolds number point-force solutions in a stratified fluid, *Phys. Rev. Lett.* **105**, 084502 (2010).
- [15] S. Okino, S. Akiyama, and H. Hanazaki, Velocity distribution around a sphere descending in a linearly stratified fluid, *J. Fluid Mech.* **826**, 759 (2017).
- [16] S. Akiyama, Y. Waki, S. Okino, and H. Hanazaki, Unstable jets generated by a sphere descending in a very strongly stratified fluid, *J. Fluid Mech.* **867**, 26 (2019).
- [17] A. Doostmohammadi and A. M. Ardekani, Reorientation of elongated particles at density interfaces, *Phys. Rev. E* **90**, 033013 (2014).
- [18] R. V. More, M. N. Ardekani, L. Brandt, and A. M. Ardekani, Orientation instability of settling spheroids in a linearly density-stratified fluid, *J. Fluid Mech.* **929**, A7 (2021).
- [19] M. M. Mrokowska, Stratification-induced reorientation of disk settling through ambient density transition, *Sci. Rep.* **8**, 412 (2018).
- [20] M. J. Mercier, S. Wang, J. Péméja, P. Ern, and A. M. Ardekani, Settling disks in a linearly stratified fluid, *J. Fluid Mech.* **885**, A2 (2020).
- [21] T. L. Mandel, D. Z. Zhou, L. Waldrop, M. Theillard, D. Kleckner, and S. Khatir, Retention of rising droplets in density stratification, *Phys. Rev. Fluids* **5**, 124803 (2020).
- [22] V. A. Shaik and A. M. Ardekani, Drag, deformation, and drift volume associated with a drop rising in a density stratified fluid, *Phys. Rev. Fluids* **5**, 013604 (2020).
- [23] M. Scase and S. Dalziel, Internal wave fields and drag generated by a translating body in a stratified fluid, *J. Fluid Mech.* **498**, 289 (1999).
- [24] N. Abaid, D. Adalsteinsson, A. Agyapong, and R. M. McLaughlin, An internal splash: Levitation of falling spheres in stratified fluids, *Phys. Fluids* **16**, 1567 (2004).
- [25] R. Camassa, L. Ding, R. M. McLaughlin, R. Overman, R. Parker, and A. Vaidya, Critical density triplets for the arrestment of a sphere falling in a sharply stratified fluid, in *Recent Advances in Mechanics and Fluid-Structure Interaction with Applications: The Bong Jae Chung Memorial Volume* (Springer, Berlin, 2022), pp. 69–91.
- [26] M. Bayareh, A. Doostmohammadi, S. Dabiri, and A. Ardekani, On the rising motion of a drop in stratified fluids, *Phys. Fluids* **25**, 103302 (2013).
- [27] H. G. Weller, G. Tabor, H. Jasak, and C. Fureby, A tensorial approach to computational continuum mechanics using object-oriented techniques, *Comput. Phys.* **12**, 620 (1998).
- [28] S. Taneda, Experimental investigation of the wake behind a sphere at low Reynolds numbers, *J. Phys. Soc. Jpn.* **11**, 1104 (1956).
- [29] N. M. Newmark, A method of computation for structural dynamics, *J. Eng. Mech. Div.* **85**, 67 (1959).
- [30] J. Deng and C. P. Caulfield, Horizontal locomotion of a vertically flapping oblate spheroid, *J. Fluid Mech.* **840**, 688 (2018).
- [31] H. Schlichting and J. Klaus, *Boundary-layer theory* (Springer Science & Business Media, Berlin, 2003).
- [32] N. Mordant and J. Pinton, Velocity measurement of a settling sphere, *Eur. Phys. J. B* **18**, 343 (2000).
- [33] J. Deng and P. Kandel, Drag force on a circular cylinder in stratified flow: A two-dimensional numerical study, *Phys. Fluids* **34**, 056601 (2022).
- [34] P. Kandel and J. Deng, Swimming in density-stratified fluid: study on a flapping foil, *Bioinspir. Biomim.* **17**, 055003 (2022).
- [35] J. Wang, J. Deng, P. Kandel, and L. Sun, Numerical study on the energy extraction performance by flapping foils in a density stratified flow, *J. Fluids Struct.* **118**, 103865 (2023).
- [36] S. Wang, P. Kandel, J. Deng, C. P. Caulfield, and S. B. Dalziel, Bouncing behaviour of a particle settling through a density transition layer, [arXiv:2301.01484](https://arxiv.org/abs/2301.01484).